

Surface Grafted Chitosan Gels. Part I. Molecular Insight into the Formation of Chitosan and Poly(acrylic acid) Multilayers

Chao Liu,[†] Esben Thormann,[‡] Per M. Claesson,^{†,§} and Eric Tyrode*,[†]

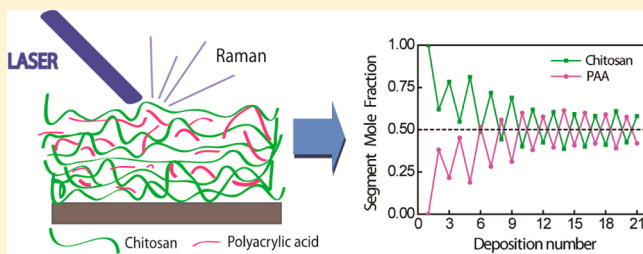
[†]School of Chemical Science and Engineering, Department of Chemistry, Surface and Corrosion Science, KTH Royal Institute of Technology, Drottning Kristinas väg 51, SE-100 44 Stockholm, Sweden

[‡]Department of Chemistry, Technical University of Denmark, Kemitorvet 207, DK-2800 Kongens Lyngby, Denmark

[§]Chemistry, Materials, and Surfaces, SP Technical Research Institute of Sweden, P.O. Box 5607, SE-114 86 Stockholm Sweden

Supporting Information

ABSTRACT: Composite polyelectrolyte multilayers of chitosan and low molecular weight poly(acrylic acid) (PAA) have been assembled by sequential adsorption as a first step toward building a surface anchored chitosan gel. Silane chemistry was used to graft the first chitosan layer to prevent film detachment and decomposition. The assembly process is characterized by nonlinear growth behavior, with different adsorption kinetics for chitosan and PAA. In situ analysis of the multilayer by means of surface sensitive total internal reflection Raman (TIRR) spectroscopy, combined with target factor analysis of the spectra, provided information regarding composition, including water content, and ionization state of weak acidic and basic groups present in the thin composite film. Low molecular weight PAA, mainly in its protonated form, diffuses into and out of the composite film during adsorption and rinsing steps. The higher molecular weight chitosan shows a similar behavior, although to a much lower extent. Our data demonstrate that the charged monomeric units of chitosan are mainly compensated by carboxylate ions from PAA. Furthermore, the morphology and mechanical properties of the multilayers were investigated *in situ* using atomic force microscopy operating in PeakForce tapping mode. The multilayer consists of islands that grow in lateral dimension and height during the build-up process, leading to close to exponentially increasing roughness with deposition number. Both diffusion in and out of at least one of the two components (PAA) and the island-like morphology contribute to the nonlinear growth of chitosan/PAA multilayers.



1. INTRODUCTION

The discovery of “volume phase transition” phenomena by Tanaka in 1978¹ inspired research on gels as functional materials. Stimuli-responsive polymer gels change volume in response to variations in the surrounding environment, leading to the modification of a number of material properties, including refractive index, elastic modulus, friction, surface tension, and adhesion. Thin films of stimuli-responsive hydrogels can be prepared using a range of methods: (1) cross-linking copolymerization, (2) cross-linking polymers with reactive groups, (3) cross-linking with high energy irradiation, (4) block copolymer self-assembly, and (5) polyelectrolyte complexation by layer-by-layer adsorption.² Responsive hydrogel thin films are of interest for applications in, e.g., membranes, micro/nanoactuators, and capsules. Making such films out of biopolymers has additional advantages in terms of, e.g., biocompatibility and biodegradability. One suitable starting material is chitin, which is one of the most abundant polysaccharides in nature, being second only to cellulose in the amount produced annually by biosynthesis.³ Chitosan is obtained by deacetylation of chitin, and it has a high content of primary amines, providing important responsive properties toward pH and ionic strength variations. Chitosan is currently

receiving a great deal of attention for microfluidics, pharmaceutical, and food applications due to its biocompatibility and biodegradability.^{4–6}

Layer-by-layer (LbL) assembly of polyelectrolyte multilayers for producing novel surface coatings has received much interest since Decher introduced the method in the early 90s.⁷ The sequential exposure of a charged surface to a polyanion solution and another polycation solution leads to the progressive buildup of thin films, often referred to as polyelectrolyte multilayers even though their intrinsic organization in many cases is not layered. The assembly process is influenced by both intrinsic properties of the polyelectrolytes and solution conditions, such as salt type, ionic strength and pH.^{8,9} Polyelectrolyte multilayers are commonly formed by attractive electrostatic interactions,¹⁰ but other interactions such as hydrogen bonding may also play an important role.¹¹ For instance, hydrogen bond driven LbL assembly has been utilized to produce temperature-responsive films.¹² The main advantages of the LbL deposition reside in the fine control of

Received: April 9, 2014

Revised: July 6, 2014

Published: July 9, 2014

chemical composition and film thickness, as well as in the fact that multilayers can be assembled on substrates of any shape. Note, however, that in highly acidic or basic solutions, LbL films containing weak acidic or basic groups have reduced stability due to imbalance between cationic and anionic polyelectrolyte charges within the film, which can lead to film detachment and decomposition.^{13–15}

Ion pairing, composition and hydration in polyelectrolyte multilayer films containing polysaccharides have been investigated by a number of techniques including quartz crystal microbalance with dissipation monitoring (QCM-D), surface plasmon resonance (SPR), ellipsometry, optical waveguide light-mode spectroscopy (OWLS), X-ray photoelectron spectroscopy (XPS), and infrared spectroscopy (FTIR).^{16–21} As for XPS, IR spectroscopy allows an unambiguous quantification of chemical groups, providing information on ion pairing and film composition. However, with the exception of the work of Picart and coworkers,¹⁶ IR spectroscopy has been limited to studying multilayers under ex situ conditions, upon drying of the film. The use of radioactive counterions has been another recent approach to track the ratio of positive to negative polymer monomeric units within a polyelectrolyte multilayer.¹⁷

In this paper we report the first study of multilayer films by total internal reflection Raman (TIRR) spectroscopy, which has been previously used to study equilibrium and/or adsorption kinetics of pure and mixed surfactant systems to solid substrates.^{22–24} This technique is capable of providing quantitative chemical information on adsorbed species and offers a number of advantages when compared with ATR-IR spectroscopy, which also makes use of evanescent waves to probe interfaces. TIRR is more surface sensitive, as it uses visible light as excitation source (i.e. shorter penetration depths). At the same time, it is easier to interpret because, first, the penetration depth does not vary with the wavelength of the vibrational transition probed, and, second, the spectral features are not distorted by the abrupt variations in the refractive index expected when approaching strong IR absorption bands. Moreover, it has a much better sensitivity for hydrocarbons relative to water due to the lower cross-section of the Raman bands from water, which makes it easier to probe *in situ* the sequential adsorption of polyelectrolytes without the need of using deuterated water.²⁵

In this report, we analyze the sequential assembly of chitosan and poly(acrylic acid) that leads to formation of a surface grafted polyelectrolyte multilayer. The effects of pH of the assembly solutions and degree of acetylation of similar multilayer films have been recently studied by Rubio and coworkers.^{26,27} Here we provide a novel molecular insight of the film growth, including the water content and ionization state of the weak acidic and basic groups within the film. The topography and mechanical properties of the film along the multilayer build-up are also characterized using atomic force microscopy (AFM). The internal chemical structure is obtained using TIRR, which allows following *in situ* the film formation process. Finally, quartz crystal microbalance with dissipation monitoring was employed to obtain information on the assembly kinetics, as well as the film hydration when combined with TIRR.

2. MATERIALS AND METHODS

2.1. Polyelectrolytes and Reagents. Chitosan (CHI, $pK_a \approx 6.0$ – 6.5^{28}) with a degree of deacetylation of 75–85% and molecular weight in the range 50 000–190 000 g/mol based on viscosity measurements,

and poly(acrylic acid) (PAA, $pK_a \approx 4.8^{28}$) with molecular weight 1800 g/mol were purchased from Sigma-Aldrich. 3-Glycidoxypolytrimethoxysilane (GPS), glacial acetic acid (HAc), acetone with 99.9% purity, sodium hydroxide (NaOH) pellets with 99.99% purity, and sodium chloride (NaCl) were used as received from Sigma-Aldrich. The water used in all experiments was purified by a Milli-Q Plus 185 system. The pH of the Milli-Q water after the treatment was ca. 5.7 and the resistivity was 18.2 MΩ·cm. The total organic carbon content of the water did not exceed 2 ppb. In contrast to chitosan, a low molecular weight PAA was chosen to facilitate the subsequent formation of the surface bound chitosan gel, where the chitosan/PAA composite film described in this work is used as scaffolding structure. For this purpose, two requirements must be fulfilled: (1) chitosan should be selectively cross-linked, and (2) it should be possible to remove PAA from the cross-linked composite layer. This is further discussed in part two of this sequence of papers.

2.2. Experimental Procedures. **2.2.1. Silanation of Silica Substrates.** The silica-coated quartz crystals and thermally oxidized silicon wafers used for the QCM-D and AFM measurements, respectively, were first treated with 2% Hellmanex (Hellma GmbH) for 30 min and then rinsed with copious amount of Milli-Q water. The custom-made fused silica hemispheres (CVI-Melles Griot) employed in the TIRR measurements were soaked in bichromatic sulfuric acid for 30 min prior to being flushed with water. The silica substrates dried under N_2 were then immersed in a closed container with 18 wt % GPS/acetone solution for 22 h and rinsed with acetone several times prior to drying at 100 °C for 1 h. The epoxide-modified substrates were used immediately after preparation.

2.2.2. Solutions and Grafting of Chitosan. The chitosan stock solution (1% w/v) was prepared in a 1% acetic acid aqueous solution, while the PAA stock solution (2000 ppm) was prepared in Milli-Q water. Before use, the solutions of chitosan and PAA were diluted to 100 and 200 ppm, respectively. The ionic strength of the polyelectrolyte solutions was adjusted to 30 mM with sodium chloride. The pH of the CHI solution was set to 6.1, and that of PAA solution to 3.7 which should favor the formation of thicker films.²⁷ The first layer of chitosan was grafted on the silanated silica surface by the amino-oxirane addition reaction.²⁹ The grafting time was 30 min. After rinsing with water, the substrates were dried in a gentle stream of N_2 gas, followed by treatment at 100 °C for 1 h.

2.2.3. Sequential Polyelectrolyte Adsorption. The adsorption time for each polyelectrolyte deposition was 4 min, and it was stopped by 1 min rinsing with a NaCl aqueous solution (30 mM, pH 5.7). The same procedure was followed in all three techniques (QCM-D, TIRR, and AFM) used for evaluating the properties of the layer.

2.3. Techniques. **2.3.1. Quartz Crystal Microbalance with Dissipation, QCM-D.** A QCM-D E4 device, from Q-sense AB (Gothenburg, Sweden) was used to simultaneously measure the resonant frequency shift, Δf , and the change in energy dissipation, ΔD , at seven different overtones. The AT-cut crystals employed had a fundamental shear frequency of 5 MHz and were coated with a 50 nm thick silica layer. To estimate the adsorbed mass and thickness of the adsorbed viscoelastic layer, the QCM-D data was analyzed using the Voigt viscoelastic model³⁰ within the software Q-tools provided by Q-sense. This model has been described in detail in the literature³⁰ (details pertinent to the present work can be found in the Supporting Information). The mass calculated from the QCM-D data is often referred to as sensed mass because it includes both coupled water and polymer mass. The sensed mass and layer thickness were obtained by fitting the Voigt model to the data obtained from overtones 3, 5, and 7. We will refer to these quantities as Voigt mass and Voigt thickness, respectively, and they were calculated using a film density of 1050 kg/m³. Note that the chosen density value has essentially no effect on the Voigt mass, whereas the Voigt thickness decreases somewhat with increasing film density. This is illustrated in the Supporting Information (Figure S3).

2.3.2. Total Internal Reflection Raman Spectroscopy. The home-built TIRR spectrometer has been described in detail elsewhere.³¹ Briefly, the excitation source is a CW 532 nm laser (Laser Quantum), which is directed to the sample position at a known polarization (S or

P) and angle of incidence. The Raman scattered light is collected using an ultralong working distance objective (Zeiss, LD-Epiplan-NEO, 50x, NA 0.55) attached to a modified Axio microscope (Zeiss). The scattered light is then passed through a polarizer with the transmission axis aligned either parallel (*x*) or perpendicular (*y*) to the plane of incidence. The scattered light is finally detected with a CCD camera (Newton 940, Andor) attached to the exit port of a spectrometer (Shamrock, Andor). The sample consisted of a hemispherical silica substrate, sealed with a Viton O-ring to the top of a custom-made glass cell.²² The use of a hemisphere helps minimizing potential aberrations in the incident beam and allows collecting the Raman scattered light in a cone of angles matched to the numerical aperture of the objective. The surface sensitivity of TIRR resides in the use of evanescent waves as excitation source.³² The penetration depth (*d*) of the squared evanescent field depends on the wavelength of the laser (λ_0), its angle of incidence from the surface normal at the interface (θ_i), and the refractive indices (*n*) of the two media (i.e., silica and solution):³³

$$d = \frac{\lambda_0}{4\pi} \left(\frac{1}{\sqrt{n_{\text{silica}}^2 \sin^2 \theta_i - n_{\text{solution}}^2}} \right) \quad (1)$$

The angle of incidence was set to 77.0°, which results in a penetration depth of ~84 nm when the solution has a refractive index similar to that of pure water ($n_{\text{silica}} = 1.46$ and $n_{\text{water}} = 1.335$). The acquisition time for each TIRR spectrum was 5 min, and all spectra were collected in contact with a 30 mM NaCl solution at 21.0 °C. The nominal power at the laser head was kept constant at 200 mW, corresponding to approximately 150 mW at the sample surface. All spectra presented here were exclusively collected under the Sy polarization combination.

The relative intensities of the TIRR bands (I_{TIRR}) are further influenced by the value of the transmitted electric field (E_{0t}) at the interface, as shown in eq 2:

$$I_{\text{TIRR}} \propto E_{0t}^2 e^{-z/d} \quad (2)$$

where *z* is the distance from the interface of the exponentially decaying field.³² E_{0t} at the interface is related to the incident electric field (E_{0i}) by the corresponding Fresnel factors, which for an S polarized beam can be written as

$$t_s = \frac{E_{0t}}{E_{0i}} = \frac{2n_{\text{silica}} \cos \theta_i}{n_{\text{silica}} \cos \theta_i + n_{\text{solution}} \cos \theta_t} \quad (3)$$

The angle of the transmitted beam (θ_t) is in turn calculated from Snell–Descartes's law:

$$n_{\text{silica}} \sin \theta_i = n_{\text{solution}} \sin \theta_t \quad (4)$$

Note that the transmitted angles are complex in TIR conditions. Equations 1–4 indicate that upon changes in the refractive index of the solution, both the penetration depth (*d*) and the transmitted electric field at the interface are expected to vary, which will have direct consequences in the absolute intensities measured by TIRR.

2.3.3. Calculating Adsorbed Amounts of Each Polyelectrolyte from the TIRR Spectra. To determine the relative proportion of chitosan and PAA from the spectra a statistical method known as target factor analysis (TFA) was used.^{34,35} The method is particularly effective when the data set can be modeled as a linear combination of constituting factors or components, which in the case concerned here, corresponds to the distinct spectral contributions from chitosan, PAA and water (bulk aqueous solution). Even though the TFA method is well established, a detailed description of the different steps followed in TFA to determine the component weights and extract absolute adsorbed amounts can be found in the Supporting Information.

2.3.4. Atomic Force Microscopy. Topographical and nanomechanical images of multilayers were recorded *in situ* by using a Multimode Nanoscope V atomic force microscope (Bruker, USA) operated in PeakForce tapping mode. The piezo is modulated at a frequency of 2 kHz, resulting in force versus separation data being generated every 0.5 ms. PeakForce tapping can be operated with a very low feedback force and is thus optimal for imaging soft or delicate

samples.³⁶ A triangular silicon nitride cantilever (Scanasyst-Fluid+, Bruker), with a nominal spring constant of 0.7 N/m, a resonance frequency of 150 kHz and a tip radius of 2 nm was used. Mechanical properties such as adhesion and deformation are extracted from the force versus separation data, simultaneously obtained over the same surface area as topography is imaged.³⁷ Images were measured at 25.0 °C in the presence of a 30 mM NaCl solution at pH 5.7. The NanoScope Analysis version 1.20 (Bruker) software was employed to analyze the images. Only the topography images were flattened to remove tilt prior to analysis. A peak force of 3.5 nN and scan rate of 0.5 Hz were used.

3. RESULTS AND DISCUSSION

3.1. Grafting of First Chitosan Layer. Chitosan readily adsorbs to the oppositely charged silica surface.⁹ However, the chitosan–surface interaction is not sufficiently strong to avoid desorption during the subsequent exposure to PAA. This can be altered by chemically grafting the first chitosan layer, through reaction of the amino groups in chitosan with the epoxide rings of a preadsorbed GPS monolayer.^{38,39} The presence of GPS on the silica substrate, with an intact epoxide ring prior to reaction with chitosan, was confirmed with TIRR as shown in Figure 1. The symmetric stretch from the

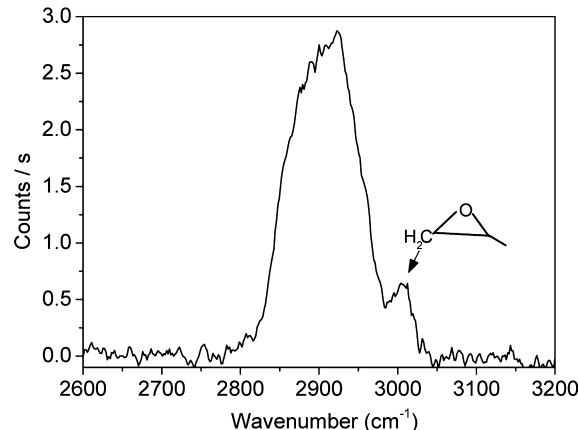


Figure 1. TIRR spectrum of the CH stretching region after silanation of the silica substrate with (3-glycidyloxypropyl)trimethoxysilane. The spectrum was collected in air using an angle of incidence of 51°.

methylene group in the epoxide ring gives rise to a characteristic band at ~3010 cm⁻¹.⁴⁰ Upon adsorption and grafting of the first layer of chitosan, this band disappeared, as expected, due to opening of the epoxide rings during the reaction.

3.2. Dynamic Events during Sequential Adsorption.

Changes in frequency and dissipation of a quartz resonator were used to track the dynamics during sequential adsorption as depicted in Figure 2a. The QCM measurements started with a single grafted layer of chitosan on the sensor surface in contact with a NaCl solution (30 mM at pH 5.7). The build-up process was continued by sequential adsorption of PAA solutions at pH 3.7 and chitosan solutions at pH 6.1, separated by an intermediate rinsing step with NaCl solutions at pH 5.7. The pH conditions, close to the respective pKa of the two polyelectrolytes, were chosen with the aim to maximize the amount of adsorb material.^{27,41}

Upon addition of each polyelectrolyte solution, a decrease in frequency and a concomitant increase in dissipation are observed. These changes are amplified as the number of deposited layer increases, suggesting nonlinear growth

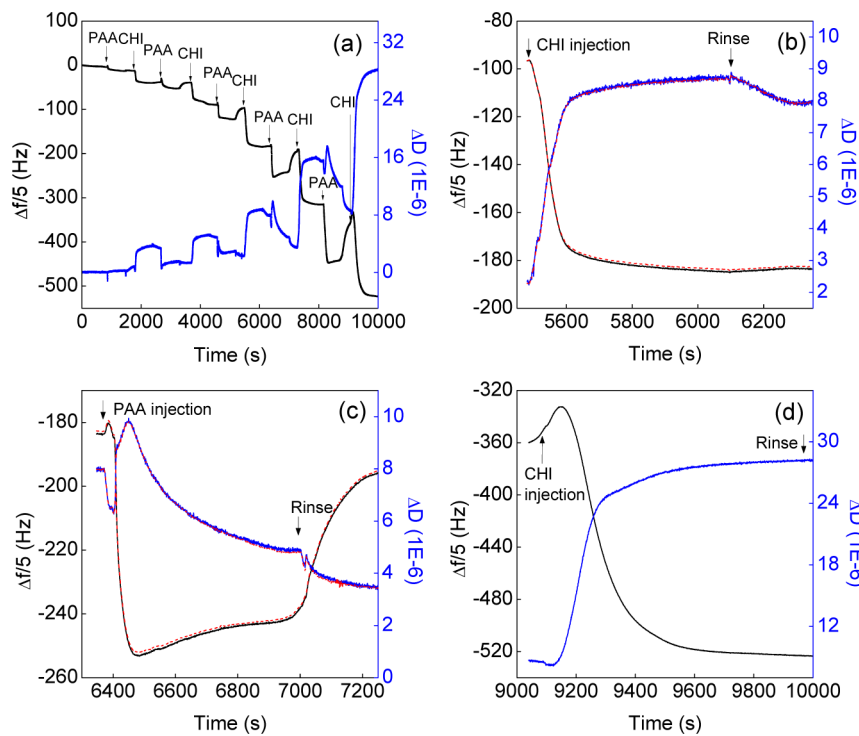


Figure 2. Frequency and dissipation changes as a function of time during (a) sequential adsorption of PAA and chitosan (CHI), (b) details observed during formation of a layer (7th) of CHI and (c) a layer (8th) of PAA (d) a layer (11th) of CHI. The measurement started by injection of PAA on a silica surface carrying a pregrafted layer of CHI. The black arrows indicate the injections of polyelectrolytes (CHI:100 ppm, PAA:200 ppm) or a rinsing solution. The frequency, dissipation, and fitting curves from the Voigt model are represented by black, blue, and red curves, respectively. The data shown are from the 5th overtone.

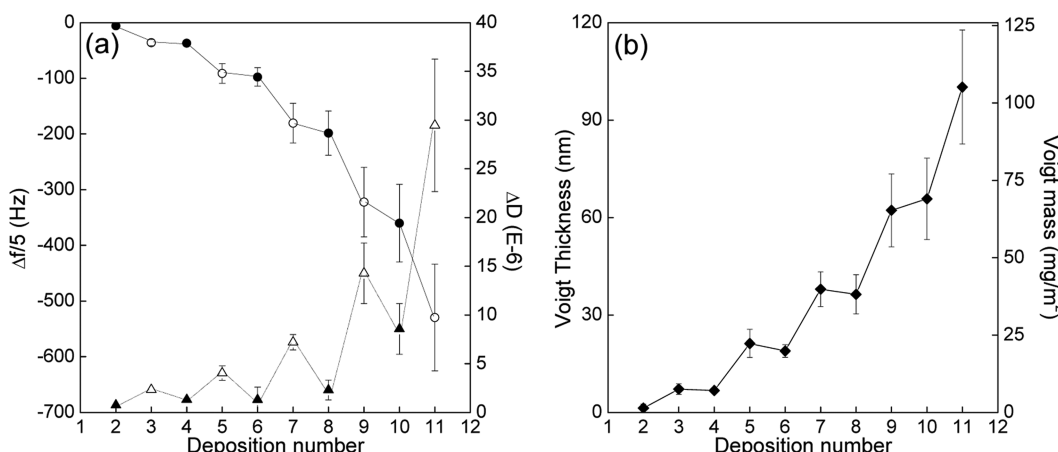


Figure 3. (a) The change in frequency (circles) and dissipation (triangles) after each adsorption and rinsing step evaluated from the QCM-D fifth overtone. Solid and open symbols represent the addition of PAA and chitosan, respectively. Error bars correspond to the standard deviation calculated from three different measurements. (b) Voigt thickness and Voigt mass estimated using the Voigt model for viscoelastic films. Data from overtones 3, 5, and 7 were used.

behavior. The chitosan/PAA multilayer becomes less rigid as it grows as evidenced by the increase in dissipation (Figure 2) and nonsuperposition of the normalized frequency for different overtones (see Supporting Information, Figure S2).

A closer inspection of the kinetic response during chitosan and PAA adsorption reveals obvious differences (see Figure 2b,c,d). The addition of chitosan, particularly in the first stages of the multilayer build up, leads to a rapid change in both frequency and dissipation followed by a plateau region, where only minor changes are observed. Upon rinsing with 30 mM NaCl solution, the dissipation decreases slightly, while hardly

any changes are detected in frequency (Figure 2b). This suggests that once the chitosan is adsorbed, it is not significantly removed by rinsing. From about deposition number 9, addition of chitosan leads to a more complex QCM-D response. Initially a net decrease in the sensed mass is observed (increase in frequency and decrease in dissipation, Figure 2d), only to later increase. Also, in this case, rinsing has limited effect (Figure 2d). In contrast, when injecting the lower molecular weight PAA, the QCM-D response is complex from the very first injection. First, a small overshoot in frequency accompanied by a sharp decrease in dissipation is usually

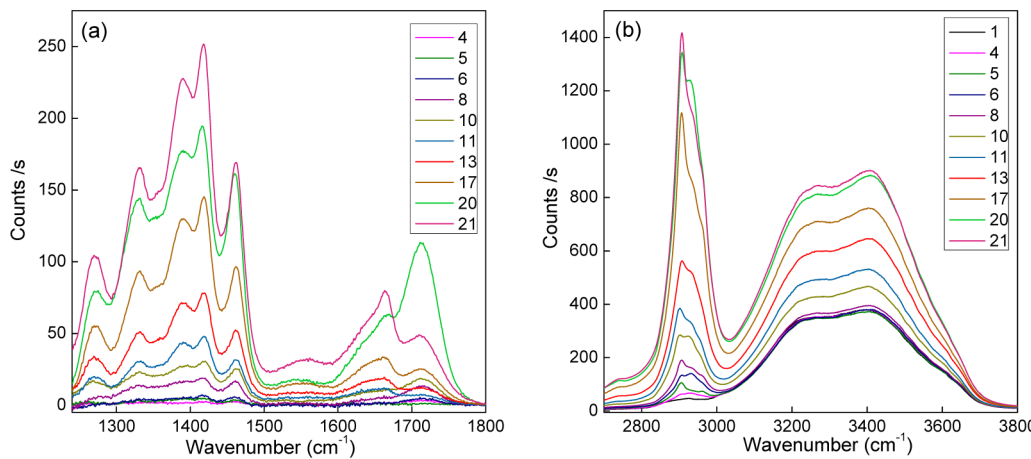


Figure 4. Selected TIRR spectra collected during the sequential adsorption process in the (a) fingerprint/double bond and (b) CH/OH stretching spectral regions. Odd and even numbered layers, correspond to the addition of chitosan and poly(acrylic acid), respectively. The spectra in panel a have been subtracted by the spectrum of Layer 1, while the raw data is presented in panel b. All spectra were collected under the S_y polarization combination.

detected (Figure 2c). Just a few tens of seconds later, the trends are inverted with the frequency showing a marked drop and the dissipation reaching a local maximum. In the final stage, the frequency is yet again observed to increase while the dissipation decreases, although this time at a much more gradual pace. Upon rinsing, this latter trend accelerates. The interpretation of these complex changes in frequency and dissipation requires additional information. This is in our study provided by TIRR, and we come back to the interpretation of the dynamics of the QCM-response in later sections.

The changes in frequency and dissipation after each adsorption step, together with the calculated film mass and thickness are summarized in Figure 3. Overall, we note a nonlinear build-up, as also observed in many other layer-by-layer studies.^{42–45} It has been argued that nonlinear growth necessarily involves the diffusion, both in and out of the film, of at least one of the constituting polyelectrolytes.⁴³ However, this interpretation has recently been put in doubt.⁴⁶ Instead, a model where the film does not grow as a homogeneous layer but rather form small islands on the surface has been proposed, and here the nonlinear growth is associated with the islands growing both in lateral dimension and in height. A closer inspection of the data in Figure 3a shows that when chitosan is added, relatively larger drops in frequency are observed (open circles) compared to those detected upon addition of PAA (solid circles). Further, the addition of PAA causes a net decrease in dissipation (solid triangles in Figure 3a), which means that the film becomes more rigid. This is likely associated with the diffusion, in and out of the layer, of the more mobile PAA that has a significantly lower molecular weight than chitosan (1800 g/mol compared to ~100.000 g/mol for chitosan). This will be further discussed in Section 3.3 once the TIRR results are presented.

3.3. Molecular Information Obtained from TIRR. The sequential adsorption (up to 21 steps) was followed *in situ* using TIRR spectroscopy. In Figure 4, a selection of the spectra recorded in two regions of interest is presented. Note that in Figure 4a, corresponding to the fingerprint/double bond stretching region, all data have been subtracted using the spectrum of the first adsorbed layer of chitosan as reference. This procedure allows removing the contributions from the silica substrate in the fingerprint region,^{22,47} as well as those

from the bending modes of bulk water present in the volume probed by the evanescent field, provided it remains constant along the multilayer buildup. In Figure 4b, however, the raw data prior to any subtraction are presented. This allows highlighting not only the contributions from the polyelectrolytes through their C–H stretching modes (2700 – 3000 cm^{-1}), but also those from water molecules within the evanescent field (O–H stretching modes extending from 3000 to 3600 cm^{-1}).

Overall, the detected signal is observed to increase with the number of deposited layers. Nonetheless, a closer inspection shows that not all bands display this monotonic behavior, with clear differences observed depending on which of the two polyelectrolytes is added last. This is, for example, the case for the peak centered at ~ 1710 cm^{-1} (Figure 4a) assigned to the carbonyl stretch $\nu(\text{C}=\text{O})$ of protonated PAA, which in spite of showing an overall increasing trend, clearly drops in intensity upon addition of chitosan (odd numbered layers). As elaborated in later sections, the decrease in intensity can be both explained by a loss of PAA molecules from the adsorbed layer and also the dissociation of the carboxylic group upon addition of chitosan. In the CH stretching region (Figure 4b) the changes are not as dramatic; however, the relative intensity of the different bands are also observed to vary depending on the number of deposited layers, reflecting changes in the relative proportion of each polyelectrolyte in the film during the build-up. The relative contribution of chitosan and PAA in the spectra can be more accurately distinguished using Target Factor Analysis (TFA).³⁴ This statistical procedure is particularly useful when no significant changes are expected in the average orientation of the adsorbates, because the area under the spectra becomes, to a good approximation, proportional to the surface coverage. Although chitosan and PAA have a number of overlapping bands in the spectral region under consideration (see Table 1 for a summary of the most important assignments), the relative differences in their peak intensities in the CH/OH stretching region are sufficient to separate their individual contributions using TFA (see Figure S1 in the Supporting Information for details).

In Figure 5a the component weights of chitosan and PAA, as well as their combined contributions as a function of deposition number are shown. These values are obtained from TFA

Table 1. Raman Assignments for Selected Bands of Chitosan and Polyacrylic Acid

| chitosan ^{48–50} | | polyacrylic acid (PAA) ^{51,52} | |
|-----------------------------------|--|---|---------------------------------|
| wavenumber (cm ⁻¹) | assignments | wavenumber (cm ⁻¹) | assignments |
| 1326 | $\tau(\text{CH}_2)$ | 1324 | $\tau(\text{CH}_2)$ |
| 1380 | HCC and HCO bending* | 1355 | $\omega(\text{CH}_2)$ |
| 1418 | HCC and HCO bending* | 1420 | $\nu_s(\text{COO}^-)$ |
| 1460 | $\delta(\text{CH}_2)$ | 1455 | $\delta(\text{CH}_2)$ |
| 1656 | $\nu(\text{C=O})$ amide | 1566 | $\nu_{\text{as}}(\text{COO}^-)$ |
| 2905 | $\nu(\text{CH})$ | 1710 | $\nu(\text{C=O})$ |
| 2945 | $\nu_s(\text{CH}_2)$ or $\nu(\text{CH})^*$ | 2878 | $\nu(\text{CH})$ |
| 3315 | $\nu_s(\text{NH}_2)$ | 2938 | $\nu_s(\text{CH}_2)$ |
| 3370 | $\nu_{\text{as}}(\text{NH}_2)$ | 2989 | $\nu_{\text{as}}(\text{CH}_2)$ |

ν , δ , ω , and τ stand for stretching, bending (scissoring), wagging, and twisting vibrational modes, respectively. The subscripts "s" and "as", denote symmetric and asymmetric modes. Asterisks "*" denote tentative assignments.

performed on the data presented in Figure 4b, and are in principle proportional to the absorbed amounts. The determination of the total concentration of PAA is facilitated in the CH stretching region because the two forms of PAA (protonated and deprotonated) exhibit practically identical spectral features in this region. This is in contrast to the fingerprint/double bond region (Figure 4a), where they show clearly distinctive bands (see Figure S4 in the Supporting Information).

A number of interesting conclusions can be extracted from Figure 5a. First, the total amount of adsorbed polyelectrolyte increases in each deposition step. The trend accelerates with the number of adsorbed layers following a nonlinear growth behavior. Second, a fraction of each polyelectrolyte is expelled from the multilayer upon adsorption of the polymer with opposite charge. This is more evident for the lower molecular weight PAA, where the trend can be tracked down to the early stages of the multilayer formation. Interestingly, chitosan also shows a similar behavior, albeit to a lower extent, becoming detectable already from deposition number 8 or even number 6. These results confirm the hypothesis that PAA diffuse in and out of the layer, as suggested by the QCM-D data reported in

Figures 2 and 3. Nonetheless, the interpretation needs to be extended to accommodate the fact that a small amount of chitosan also leaves the multilayer during PAA addition.

3.4. Adsorbed Amounts from TIRR. The adsorbed amounts of the individual polyelectrolytes can be estimated from the component weight data as described in the experimental section. The procedure is straightforward provided: first, the spectral features of the polyelectrolyte in the adsorbed layer and in the bulk reference solution are similar, and, second, the penetration depth of the exciting evanescent field remains approximately constant. Although, the former condition is met for both PAA and chitosan, the latter requires further consideration.

Due to the relatively higher refractive index of the adsorbed polymer multilayer compared to the aqueous bulk solution, the penetration depth of the evanescent field is expected to increase as the build-up process proceeds (eq 1). This effect becomes significant as the film thickens, particularly when approaching values comparable to those of the penetration depth. Moreover, the changes in the refractive index caused by the adsorbed film will also influence the absolute value of the electric field at the interface, as predicted by the Fresnel equations (eq 2 and eq 3). One obvious consequence of an extended penetration depth is that the absolute intensities of the spectral bands associated with water would increase, as more molecules from the bulk are probed by the then also stronger evanescent field. This is indeed observed, starting from layer number 10, in the recorded TIRR data shown in Figure 4b. The relative increase of the water signal with deposition number is quantitatively summarized in the inset of Figure 5a, reaching nearly 3 times the starting value at the end of the deposition process. Had the penetration depth of the evanescent field remained constant, the relative contribution of water molecules to the spectra would have, if anything, decreased.

Concurrently, the bands associated with the polyelectrolytes in the adsorbed layer are enhanced due to the increase of the electric field intensity at the silica/film interface, which results in an overestimation of the adsorbed amount for each polyelectrolyte calculated assuming a constant penetration depth. To take into account the changes in Raman intensity due to both a varying penetration depth and electric field intensity at the interface, we use, as a first approximation, a two layer model consisting of silica and a water equivalent phase of

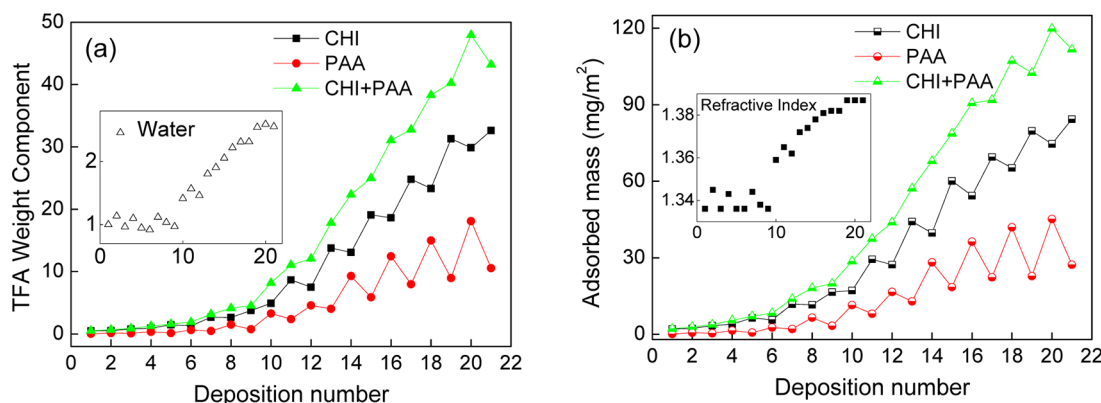


Figure 5. (a) Target factor analysis weight component for chitosan (CHI) and PAA as a function of deposition number evaluated from peaks in the CH/OH stretching region. The corresponding weight component for water is shown in the inset. (b) Calculated adsorbed amounts for CHI and PAA obtained from the TIRR data. The refractive index of the rarer medium estimated from a two layer model is also shown in the inset. Odd and even numbered layers correspond to the deposition of chitosan and PAA, respectively.

varying index of refraction, to estimate the change in refractive index (Supporting Information, Figure S5) required to match the measured increase in water signal (inset in Figure 5a). The results obtained are presented in the inset of Figure 5b, which are used to calculate the adsorbed masses of chitosan and PAA starting from layer number 10. At this point it is worth noting the limitations of the two layer model for describing the physical system; in particular, the fact that the thickness of adsorbed polyelectrolyte film, which varies depending on the number of deposited layers, is not explicitly considered. The modeling could in principle be improved using a three-layer model.^{53,54} However, the number of additional parameters and assumptions required (i.e. homogeneous film) limits the benefits of this approach for the set of data collected.

The calculated adsorbed masses in mg/m² for each polyelectrolyte are shown in Figure 5b. The curves follow the general trends already discussed above in terms of weight components. It is worth noting, however, that the growth in adsorbed mass actually displays two distinctive linear regions, with the interlude somewhere between deposition number 9 and 10. There are also two interesting features that are now apparent at the end of the deposition process (at and above layer 16). First, the overall mass deposition rate appears to clearly decelerate, and second, the total amount of polyelectrolyte adsorbed does no longer increase for each deposition step. This could initially be interpreted as another change in the growth behavior; however, the AFM studies described in Section 3.8 suggest otherwise. The apparent change in growth rate is instead most certainly a consequence of the limited probing depth of the electric field, losing sensitivity for newly deposited material as the average film thickness exceeds the penetration depth. Consequently, the chitosan and PAA adsorbed amounts reported in Figure 5b for deposition layer number 16 and above are underestimated.

3.5. Layer Hydration. In contrast to QCM-D, TIRR measures the mass of the adsorbed polyelectrolytes. The amount of water in the film can then be extracted by comparing the total adsorbed mass from TIRR with the Voigt mass obtained with QCM-D. The water content in the film as a function of deposition number for up to 11 layers (largest number of depositions measured with QCM-D) is shown in Figure 6. Overall, the level of hydration is in the order of 60%, although the data also indicates that during the early stages of

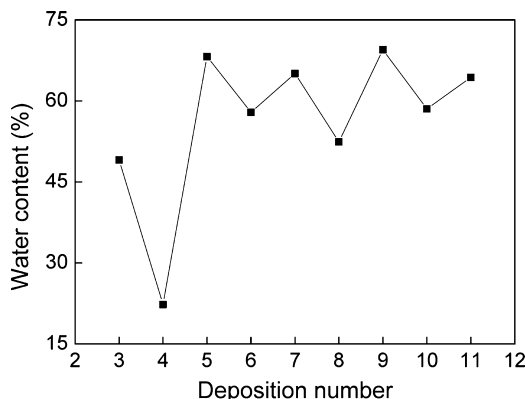


Figure 6. Water weight percentage in the adsorbed film as a function of the number of depositions, calculated by combining QCM-D and TIRR results. Odd and even numbered layers correspond to the deposition of chitosan and PAA, respectively.

the multilayer formation the films are significantly drier. Interestingly, when PAA is added last, the film systematically shows lower water contents (even numbered layers in Figure 6). This demonstrates that a certain amount of water is released upon introduction of PAA, resulting in a more compact and rigid film as clearly is manifested in the QCM-D data (Figure 3).

3.6. Polyelectrolyte Monomeric Unit Mole Fractions.

The chitosan and PAA monomeric unit mole fractions for each deposition step are shown in Figure 7, as calculated based on

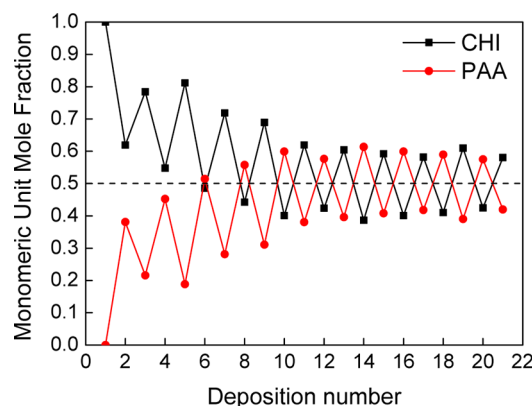


Figure 7. Monomeric unit mole fraction (including charged and uncharged fractions) as a function of deposition number obtained from the TIRR data. The dashed line at 0.5 is a guide to the eyes. Odd and even numbered layers correspond to the deposition of chitosan and PAA, respectively.

the data shown in Figure 5. Although determined from the calculated adsorbed masses (see Experimental Procedures section for details), the mole fractions are more reliable because they are less sensitive to potential experimental errors associated with the determination of the Raman absolute intensities. Moreover, they are also independent of the model chosen to account for the changes in the penetration depth of the electric field. Figure 7 helps visualizing a number of interesting features. First, the polyelectrolyte monomeric unit mole fractions oscillate up and down after each subsequent deposition, with chitosan and PAA showing opposite trends, confirming that each polyelectrolyte is deposited in turns. Second and more importantly, the molecular fraction of chitosan in the film shows a downward trend up to layer number 10, stabilizing afterward around a molar fraction of 0.5. The lower proportion of PAA in the early stages of the multilayer formation is most probably a consequence of the underlying solid substrate. Fused silica is negatively charged at pHs above 2–3.⁵⁵ Thus, it will have a negative impact on the amount of polyanion (PAA) adsorbed as long as its surface charges are not fully screened by the adsorbed chitosan. Connecting back to Figure 5b, the interlude between the two linear growth regions at deposition number 9 or 10 coincides with the stabilization of the molar fractions, indicating that complete neutralization of the silica charge may play an important role in the growth acceleration. The fact that it is not until layer number 8 or 10, corresponding in principle to an average thickness of 40 nm or more (Figure 3b), that an equilibrium value is reached implies that the adsorbed film is not homogeneous (had it been homogeneous, the charges from silica would have been screened by a much thinner film), a

hypothesis that is confirmed by the AFM measurements shown below.

The data presented in Figure 7 shows the total molar fraction for each polyelectrolyte in the film, which includes both charged and uncharged segments. This is not to be confused with the overcompensation mechanism, which also depends on the degree of protonation of chitosan and PAA.

3.7. Overcompensation and Complexation. Charge overcompensation during each deposition step is, in principle, a requirement for sequential adsorption of two oppositely charged polyelectrolytes.⁴⁴ However, charge overcompensation is not anticipated if only electrostatic interactions are taken into account, because in contrast to neutralization, charging a surface leads to an increase of electrostatic free energy. The main driving force facilitating adsorption is the entropic gain associated with the release of counterions up to charge neutralization, but the adsorption process also results in an entropy decrease due to the smaller number of chain conformations. The adsorbed polyelectrolyte chains are thus likely to form some loops and tails, with associating counterions, at the interface. This contributes to charge overcompensation (by the polyelectrolyte segments), which allows multilayer build-up. Non-Coulomb interactions between the polyelectrolytes due to, e.g., hydrogen bonds, van der Waals interactions or hydrophobic interactions are also expected to contribute to charge overcompensation.^{25,56,57} TIRR can provide a deeper insight into this mechanism by targeting the chargeable groups in the polyelectrolytes, specifically the carboxylic ($\text{COOH} \leftrightarrow \text{COO}^-$) and amino ($\text{NH}_2 \leftrightarrow \text{NH}_3^+$) groups from PAA and chitosan, respectively.

As shown in Table 1, the carbonyl group and carboxylate groups from PAA give rise to distinctive and separable bands. However, the asymmetric carboxylate stretch, $\nu_{as}(\text{COO}^-)$ is very weak in Raman, while the symmetric carboxylate stretch, $\nu_s(\text{COO}^-)$ closely overlaps with a band from chitosan (Table 1 and Figure S4), making impractical a direct quantitative determination of the adsorbed amount from charged PAA monomeric units. On the other hand, the carbonyl stretch, $\nu(\text{C=O})$, is free from overlapping bands (Figure S4) and can be used for determining the adsorbed amount of the protonated form of PAA, by employing TFA and following the calibration procedure mentioned above. The amount of deprotonated PAA monomeric units is then obtained by subtracting the amount of protonated PAA from the total amount of PAA computed from the CH stretching region (Figure 5b). The adsorbed amounts of the protonated and deprotonated forms of PAA monomeric units as a function of layer deposition number are shown in Figure 8. It can be concluded that it is mainly the amount of protonated PAA monomeric units that decreases upon deposition of chitosan (odd numbered deposition), with the amount of deprotonated PAA monomeric units remaining fairly constant in the adsorbed film, most probably forming a complex with chitosan. Moreover, it is also mainly the amount of noncharged PAA monomeric units that increases upon deposition of PAA (even numbered depositions). The proportion of protonated PAA monomeric units in the film oscillates between approximately 25% and 50% between odd and even numbered layers, except during the early stages of the build-up process when it is the dominant form (see inset in Figure 8). Having a larger proportion of noncharged PAA monomeric units in the first layers is certainly a consequence of the underlying negatively charged silica substrate.

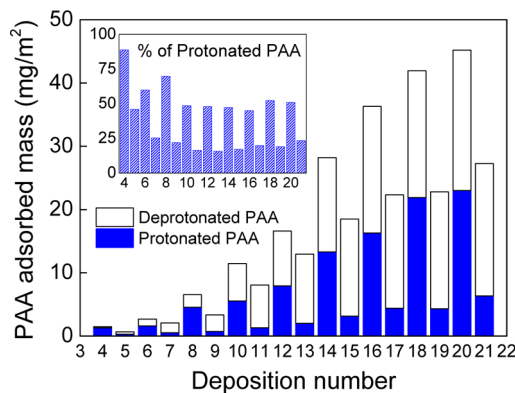


Figure 8. Calculated adsorbed amounts for protonated and deprotonated monomeric units of PAA as a function of number of deposited layers. Inset: percentage of protonated PAA monomeric units in the adsorbed layer along the build-up process. Odd and even numbered layers correspond to the deposition of chitosan and PAA, respectively.

If PAA–chitosan complexes are formed, association between COO^- from PAA and NH_3^+ from chitosan is expected. The NH_3^+ group from chitosan gives rise to rather weak and broad bands in Raman, which impairs any possibility for direct determination. Nonetheless, the adsorbed amount of the uncharged form of chitosan can, in principle, be obtained by targeting the sharp NH stretching vibrations, $\nu_s(\text{NH}_2)$ and $\nu_a(\text{NH}_2)$, from the amino group (Table 1). In spite of overlapping with the broad OH stretching bands from water, the NH modes should be easily detectable in the thicker films. They are, however, not observed at any stage of the film formation process (Figure 4b). A proof that these bands are indeed detectable can be found in part two of this series of papers, where spectra are presented upon removal of PAA from the chitosan gel.⁵⁸ The limit of detectability of these NH stretching modes can be established to be <15% for deposition number 10, reducing to less than 5% at the end of the build-up process based on the existing peak in the cross-linked chitosan gel spectra.⁵⁸ The results indicate that in contrast to PAA, the large majority of chargeable chitosan monomeric units (D-glucosamine) in the film, if not all, are found in their charged form (NH_3^+), and this regardless of whether chitosan or PAA is deposited last. Considering that approximately ~80% of chitosan is deacetylated (with the remaining 20% consisting of acetylglucosamine units, thus not contributing to the charge) it can be concluded that a very large fraction (from approximately 70 to even 100%) of the charged chitosan units are complexated with deprotonated PAA (intrinsic compensation mechanism¹⁷). This is particularly true from layers number 10 and above, because at the early stages of the multilayer formation, chitosan charged units can also interact with the negatively charged silica substrate. Accordingly, charge compensation by counterions (extrinsic compensation mechanism) appears to be small in the chitosan/PAA multilayer system (see Figure S6 in the Supporting Information showing the monomer mole fractions of charged segments as a function of deposition number).

3.8. Structural Information Obtained with AFM. AFM topography images at certain stages of the film formation process are provided in Figure 9. The images show that already from the first layer (layer 1 consisting of grafted chitosan), the adsorbed film is inhomogeneous, with further adsorption

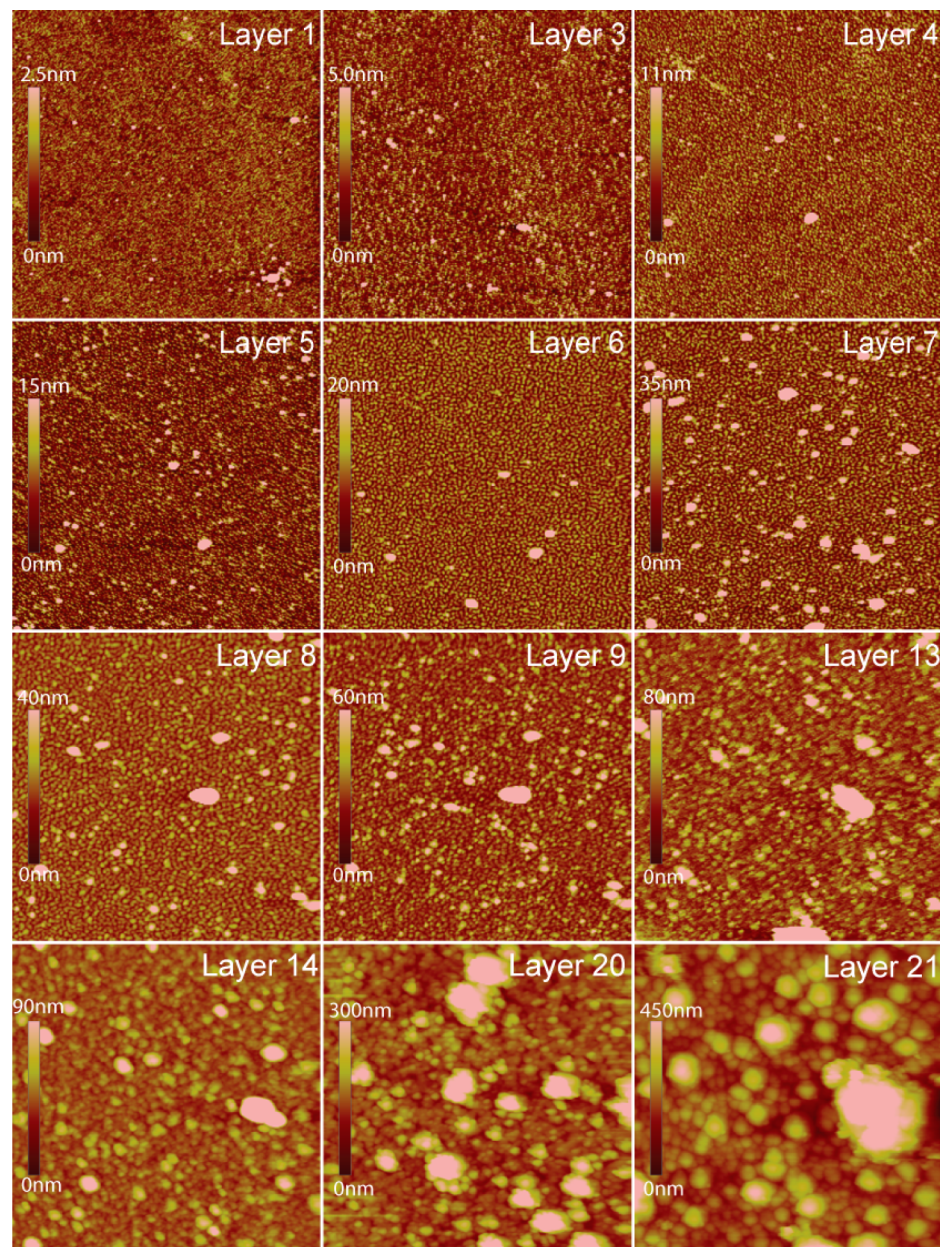


Figure 9. AFM topography images of some specific deposited layers (deposition numbers provided in the images) in 30 mM NaCl at pH 5.7. Note the change in the height bar scales along the build-up process. Image size: $10 \times 10 \mu\text{m}^2$. Odd and even numbered layers correspond to the deposition of chitosan and PAA, respectively.

mainly occurring in those areas where material had previously been deposited. From topography alone it is difficult to ascertain from the images when the underlying silica substrate is fully covered. However, after approximately six or seven deposited layers, the surface appears to be completely covered by isolated islands. Surface material properties in terms of tip-sample adhesion and sample deformation illustrates that polymer material also is found between the island (see images in Supporting Information Figure S7). This conclusion is based on the magnitude of adhesion and deformation between the islands, which are distinctively different from the properties of uncoated silica. As the build-up proceeds, the film gets rougher (Figure 10) with aggregates growing in size in both lateral and vertical directions. This process starts from layer 9 until large aggregates eventually fully cover the surface (see for example layers 20 and 21 in Figure 9). This transition in morphology

occurs in the region where the growth behavior changes (see Figures 3 and 5).

The root-mean-square roughness depicted in Figure 10 is seen to increase with the number of deposited layers. This is in contrast to what has been reported for an exponentially growing film of polyglutamic acid and polylysine (PGA/PLL), where the roughness was observed to remain essentially constant after five deposited layers.⁴² This difference highlights the possibility of having different build-up mechanisms in nonlinear growing films. In our case the chitosan/PAA system involves both diffusion in and out of the layer and growth of islands, where both mechanisms have been shown to result in nonlinear build-up.⁴⁶

At this point it is worth noting that when properties of surface layers are evaluated using most techniques, such as QCM-D, ellipsometry, dual polarization interferometry, or

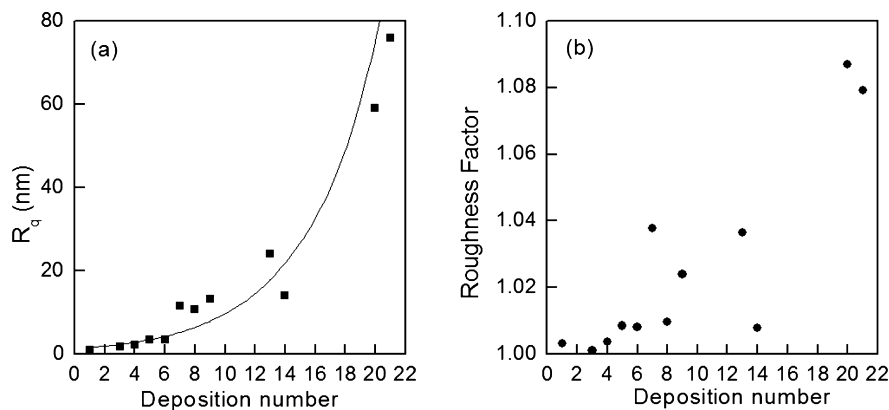


Figure 10. Root mean square roughness (a) and roughness factor (b) as a function of deposition number obtained from the AFM images, size: $10 \times 10 \mu\text{m}^2$. The line in panel a following an exponential pattern is just a guide to the eye. Odd and even numbered layers correspond to deposition of chitosan and PAA, respectively.

surface plasmon resonance, homogeneous layer models are applied to evaluate the data. As seen in Figure 9, reality is often more complex, and inhomogeneities are often observed. Thus, the properties returned by the analysis, in our case Voigt modeling of QCM-D data, are those of a homogeneous layer that would result in a similar measurement response as the real inhomogeneous surface layer. To emphasize this, we refer to the modeled data as “Voigt mass” and “Voigt thickness”. In reality, both the local mass of the film and its local thickness vary with the surface coordinates, and thus values reported should be used with some care.

SUMMARY AND CONCLUDING REMARKS

We have followed the buildup of polyelectrolyte multilayers of chitosan and low molecular weight PAA *in situ* using QCM-D, TIRR, and AFM PeakForce tapping. The first chitosan layer was grafted to the silica substrate to increase the stability of the films formed. The data from QCM-D and TIRR show that the film does not display linear growth, with the growth rate increasing after about 8–9 depositions. This change in growth behavior correlates with the appearance of large aggregates in the AFM images and the full screening of the negative charges of the underlying silica substrate.

TIRR clearly demonstrates that PAA, particularly in its protonated form, diffuses in and out of the multilayer. On the other hand, AFM shows evidence of a nonuniform growth with the formation of island-like aggregates at the surface. Consequently, during the buildup of the chitosan–PAA multilayer, the distinctive features of the two, in principle, competing models^{43,46,57} proposed for explaining the nonlinear growth behavior are observed, suggesting that these models are not necessarily mutually exclusive.

The TIRR spectra not only proved the incorporation and expulsion of PAA within the multilayer, but also that of chitosan, albeit to a lower extent. Moreover, the water content in the film up to the first 10 deposited layers, estimated by combining QCM-D and TIRR data, was found to oscillate around 60%, being somewhat higher when chitosan was deposited last. The chemical specificity of TIRR also allowed determining the fraction of charged PAA and chitosan present in the adsorbed film, demonstrating that the fraction of deprotonated carboxylate groups increases each time chitosan is added, whereas chitosan is predominantly, if not exclusively, found in its protonated form. A charge balance calculation

shows that the large majority of the protonated amine groups are charge compensated by carboxylate groups from PAA.

The inhomogeneous film with large islands produced by the multilayer approach constitutes a scaffold for the synthesis of a surface grafted chitosan gel. The gel is produced by first cross-linking chitosan monomeric units, followed by the removal of unbound PAA. This process, as well as the surface-bound gel responsiveness to changes in solution conditions, is described in detail in part II of this series of papers.⁵⁸

ASSOCIATED CONTENT

Supporting Information

Voigt modeling of the QCM-D data, description of steps followed in Target Factor Analysis to determine adsorbed polyelectrolyte masses, QCM-D curves at different overtones including parameters used in the Voigt modeling of film mass and thickness, bulk Raman spectra from protonated and deprotonated PAA, estimation of the refractive index in the two layer model for determining the absolute mass from the TIR Raman data, mole fraction of charged monomeric units (overcompensation) as a function of deposited layer obtained by TIR Raman, and Surface Material properties of the multilayer obtained by AFM. This material is available free of charge via the Internet at <http://pubs.acs.org/>.

AUTHOR INFORMATION

Corresponding Author

*E-mail: tyrode@kth.se.

Notes

The authors declare no competing financial interest.

ACKNOWLEDGMENTS

All authors acknowledge individual financial support from the Swedish Research Council, VR. E.Th. and E.Ty. also acknowledge support from the Swedish Foundation for Strategic Research (SSF) through the programs “Microstructure, Corrosion and Friction Control” and “Future Research Leaders-5”, respectively.

REFERENCES

- (1) Tanaka, T. Collapse of Gels and the Critical Endpoint. *Phys. Rev. Lett.* **1978**, *40* (12), 820–823.
- (2) Tokarev, I.; Minko, S. Stimuli-Responsive Hydrogel Thin Films. *Soft Matter* **2009**, *5* (3), 511–524.

- (3) Cohen, E. Chitin Biochemistry: Synthesis and Inhibition. *Annu. Rev. Entomol.* **1987**, *32* (1), 71–93.
- (4) Koev, S. T.; Dykstra, P. H.; Luo, X.; Rubloff, G. W.; Bentley, W. E.; Payne, G. F.; Ghodssi, R. Chitosan: An Integrative Biomaterial for Lab-on-a-Chip Devices. *Lab Chip* **2010**, *10* (22), 3026–3042.
- (5) Yi, H.; Wu, L.-Q.; Bentley, W. E.; Ghodssi, R.; Rubloff, G. W.; Culver, J. N.; Payne, G. F. Biofabrication with Chitosan. *Biomacromolecules* **2005**, *6* (6), 2881–2894.
- (6) Shahidi, F.; Arachchi, J. K. V.; Jeon, Y.-J. Food Applications of Chitin and Chitosans. *Trends Food Sci. Technol.* **1999**, *10* (2), 37–51.
- (7) Decher, G. Fuzzy Nanoassemblies: Toward Layered Polymeric Multicomposites. *Science* **1997**, *277* (5330), 1232–1237.
- (8) Feldtöö, Z.; Varga, I.; Blomberg, E. Influence of Salt and Rinsing Protocol on the Structure of PAH/PSS Polyelectrolyte Multilayers. *Langmuir* **2010**, *26* (22), 17048–17057.
- (9) Lundin, M.; Solaqa, F.; Thormann, E.; Macakova, L.; Blomberg, E. Layer-by-Layer Assemblies of Chitosan and Heparin: Effect of Solution Ionic Strength and pH. *Langmuir* **2011**, *27* (12), 7537–7548.
- (10) Lee, G.; Shin, Y.-H.; Son, J. Y. Formation of Self-Assembled Polyelectrolyte Multilayer Nanodots by Scanning Probe Microscopy. *J. Am. Chem. Soc.* **2009**, *131* (5), 1634–1635.
- (11) Sukhishvili, S. A.; Granick, S. Layered, Erasable Polymer Multilayers Formed by Hydrogen-Bonded Sequential Self-Assembly. *Macromolecules* **2002**, *35* (1), 301–310.
- (12) Kharlampieva, E.; Kozlovskaya, V.; Tyutina, J.; Sukhishvili, S. A. Hydrogen-Bonded Multilayers of Thermoresponsive Polymers. *Macromolecules* **2005**, *38* (25), 10523–10531.
- (13) Dubas, S. T.; Schlenoff, J. B. Polyelectrolyte Multilayers Containing a Weak Polyacid: Construction and Deconstruction. *Macromolecules* **2001**, *34* (11), 3736–3740.
- (14) Sukhishvili, S. A.; Granick, S. Layered, Erasable, Ultrathin Polymer Films. *J. Am. Chem. Soc.* **2000**, *122* (39), 9550–9551.
- (15) Mendelsohn, J. D.; Barrett, C. J.; Chan, V. V.; Pal, A. J.; Mayes, A. M.; Rubner, M. F. Fabrication of Microporous Thin Films from Polyelectrolyte Multilayers. *Langmuir* **2000**, *16* (11), 5017–5023.
- (16) Crouzier, T.; Picart, C. Ion Pairing and Hydration in Polyelectrolyte Multilayer Films Containing Polysaccharides. *Biomacromolecules* **2009**, *10* (2), 433–442.
- (17) Ghostine, R. A.; Markarian, M. Z.; Schlenoff, J. B. Asymmetric Growth in Polyelectrolyte Multilayers. *J. Am. Chem. Soc.* **2013**, *135* (20), 7636–7646.
- (18) Dubas, S. T.; Schlenoff, J. B. Factors Controlling the Growth of Polyelectrolyte Multilayers. *Macromolecules* **1999**, *32* (24), 8153–8160.
- (19) Abdelkebir, K.; Gaudiere, F.; Morin-Grognat, S.; Coquerel, G.; Labat, B.; Atmani, H.; Ladam, G. Evidence of Different Growth Regimes Coexisting within Biomimetic Layer-by-Layer Films. *Soft Matter* **2011**, *7* (19), 9197–9205.
- (20) Crouzier, T.; Boudou, T.; Picart, C. Polysaccharide-Based Polyelectrolyte Multilayers. *Curr. Opin. Colloid Interface Sci.* **2010**, *15* (6), 417–426.
- (21) Almodóvar, J.; Place, L. W.; Gogolski, J.; Erickson, K.; Kipper, M. J. Layer-by-Layer Assembly of Polysaccharide-Based Polyelectrolyte Multilayers: A Spectroscopic Study of Hydrophilicity, Composition, and Ion Pairing. *Biomacromolecules* **2011**, *12* (7), 2755–2765.
- (22) Tyrode, E.; Rutland, M. W.; Bain, C. D. Adsorption of CTAB on Hydrophilic Silica Studied by Linear and Nonlinear Optical Spectroscopy. *J. Am. Chem. Soc.* **2008**, *130* (51), 17434–17445.
- (23) Woods, D. A.; Petkov, J.; Bain, C. D. Surfactant Adsorption Kinetics by Total Internal Reflection Raman Spectroscopy. 2. CTAB and Triton X-100 Mixtures on Silica. *J. Phys. Chem. B* **2011**, *115* (22), 7353–7363.
- (24) Grenoble, Z.; Baldelli, S. Adsorption of Benzylidimethylhexadecylammonium Chloride at the Hydrophobic Silica–Water Interface Studied by Total Internal Reflection Raman Spectroscopy: Effects of Silica Surface Properties and Metal Salt Addition. *J. Phys. Chem. B* **2013**, *117* (34), 9882–9894.
- (25) Picart, C.; Lavalle, P.; Hubert, P.; Cuisinier, F. J. G.; Decher, G.; Schaaf, P.; Voegel, J. C. Buildup Mechanism for Poly(l-lysine)/Hyaluronic Acid Films onto a Solid Surface. *Langmuir* **2001**, *17* (23), 7414–7424.
- (26) Guzman, E.; Chulia-Jordan, R.; Ortega, F.; Rubio, R. G. Influence of the Percentage of Acetylation on the Assembly of LbL Multilayers of Poly(acrylic acid) and Chitosan. *Phys. Chem. Chem. Phys.* **2011**, *13* (40), 18200–18207.
- (27) Guzmán, E.; Cavallo, J. A.; Chuliá-Jordán, R.; Gómez, C. s.; Strumia, M. C.; Ortega, F.; Rubio, R. n. G. pH-Induced Changes in the Fabrication of Multilayers of Poly(acrylic acid) and Chitosan: Fabrication, Properties, and Tests as a Drug Storage and Delivery System. *Langmuir* **2011**, *27* (11), 6836–6845.
- (28) Argüelles-Monal, W.; Peniche-Covas, C. Study of the interpolyelectrolyte reaction between chitosan and carboxymethyl cellulose. *Makromol. Chem., Rapid Commun.* **1988**, *9* (10), 693–697.
- (29) Liu, Y. L.; Su, Y. H.; Lai, J. Y. In Situ Crosslinking of Chitosan and Formation of Chitosan–Silica Hybrid Membranes with Using Gamma-Glycidoxypolytrimethoxysilane as a Crosslinking Agent. *Polymer* **2004**, *45* (20), 6831–6837.
- (30) Voinova, M. V.; Rodahl, M.; Jonson, M.; Kasemo, B. Viscoelastic Acoustic Response of Layered Polymer Films at Fluid–Solid Interfaces: Continuum Mechanics Approach. *Phys. Scr.* **1999**, *59* (5), 391–396.
- (31) Tyrode, E.; Liljeblad, J. F. D. Water Structure Next to Ordered and Disordered Hydrophobic Silane Monolayers: A Vibrational Sum Frequency Spectroscopy Study. *J. Phys. Chem. C* **2013**, *117* (4), 1780–1790.
- (32) Woods, D. A.; Bain, C. D. Total Internal Reflection Raman Spectroscopy. *Analyst* **2012**, *137* (1), 35–48.
- (33) Lipson, S. G.; Lipson, H.; Tannhauser, D. S. *Optical Physics*, 3rd ed.; University Press: Cambridge, U.K., 1995.
- (34) Malinowski, E. R. *Factor Analysis in Chemistry*, 3rd ed.; Wiley: New York, 2002.
- (35) Woods, D. A.; Petkov, J.; Bain, C. D. Surfactant Adsorption Kinetics by Total Internal Reflection Raman Spectroscopy. 1. Pure Surfactants on Silica. *J. Phys. Chem. B* **2011**, *115* (22), 7341–7352.
- (36) Rico, F.; Su, C.; Scheuring, S. Mechanical Mapping of Single Membrane Proteins at Submolecular Resolution. *Nano Lett.* **2011**, *11* (9), 3983–3986.
- (37) Duner, G.; Thormann, E.; Dedinaite, A.; Claesson, P. M.; Matyjaszewski, K.; Tilton, R. D. Nanomechanical mapping of a high curvature polymer brush grafted from a rigid nanoparticle. *Soft Matter* **2012**, *8* (32), 8312–8320.
- (38) Wong, A.; Krull, U. Surface Characterization of 3-Glycidoxypolytrimethoxysilane Films on Silicon-Based Substrates. *Anal. Bioanal. Chem.* **2005**, *383* (2), 187–200.
- (39) Piehler, J.; Brecht, A.; Valiokas, R.; Liedberg, B.; Gauglitz, G. A High-Density Poly(ethylene glycol) Polymer Brush for Immobilization on Glass-Type Surfaces. *Biosens. Bioelectron.* **2000**, *15* (9–10), 473–481.
- (40) Polavarapu, P. L.; Hess, J. B. A.; Schaad, L. J. Vibrational Spectra of Epoxypropane. *J. Chem. Phys.* **1985**, *82* (4), 1705–1710.
- (41) Schoeler, B.; Kumaraswamy, G.; Caruso, F. Investigation of the Influence of Polyelectrolyte Charge Density on the Growth of Multilayer Thin Films Prepared by the Layer-by-Layer Technique. *Macromolecules* **2001**, *35* (3), 889–897.
- (42) Lavalle, P.; Gergely, C.; Cuisinier, F. J. G.; Decher, G.; Schaaf, P.; Voegel, J. C.; Picart, C. Comparison of the Structure of Polyelectrolyte Multilayer Films Exhibiting a Linear and an Exponential Growth Regime: An in Situ Atomic Force Microscopy Study. *Macromolecules* **2002**, *35* (11), 4458–4465.
- (43) Lavalle, P.; Picart, C.; Mutterer, J.; Gergely, C.; Reiss, H.; Voegel, J.-C.; Senger, B.; Schaaf, P. Modeling the Buildup of Polyelectrolyte Multilayer Films Having Exponential Growth. *J. Phys. Chem. B* **2003**, *108* (2), 635–648.
- (44) Steitz, R.; Jaeger, W.; Klitzing, R. v. Influence of Charge Density and Ionic Strength on the Multilayer Formation of Strong Polyelectrolytes. *Langmuir* **2001**, *17* (15), 4471–4474.

- (45) Hoda, N.; Larson, R. G. Modeling the Buildup of Exponentially Growing Polyelectrolyte Multilayer Films. *J. Phys. Chem. B* **2009**, *113* (13), 4232–4241.
- (46) Haynie, D. T.; Cho, E.; Waduge, P. “In and Out Diffusion” Hypothesis of Exponential Multilayer Film Buildup Revisited. *Langmuir* **2011**, *27* (9), 5700–5704.
- (47) Lee, C. S.; Bain, C. D. Raman Spectra of Planar Supported Lipid Bilayers. *Biochim. Biophys. Acta, Biomembr.* **2005**, *1711* (1), 59–71.
- (48) Wiley, J. H.; Atalla, R. H. Band Assignments in the Raman Spectra of Celluloses. *Carbohydr. Res.* **1987**, *160* (0), 113–129.
- (49) Pearson, F. G.; Marchessault, R. H.; Liang, C. Y. Infrared Spectra of Crystalline Polysaccharides. V. Chitin. *J. Polym. Sci.* **1960**, *43* (141), 101–116.
- (50) Blackwell, J. Infrared and Raman Spectroscopy of Cellulose. In *Cellulose Chemistry and Technology*; Arthur, J. C., Jr., Ed.; American Chemical Society: Washington, DC, 1977; Vol. 48, pp 206–218.
- (51) Bardet, L.; Cassanas-Fabre, G.; Alain, M. Étude de la Transition Conformationnelle de l’Acide Polyacrylique Syndiotactique en Solution Aqueuse par Spectroscopie de Vibration. *J. Mol. Struct.* **1975**, *24* (1), 153–164.
- (52) Gupta, M. K.; Bansil, R. Laser Raman Spectroscopy of Polyacrylamide. *J. Polym. Sci., Polym. Phys. Ed.* **1981**, *19* (2), 353–360.
- (53) Citra, M. J.; Axelsen, P. H. Determination of Molecular Order in Supported Lipid Membranes by Internal Reflection Fourier Transform Infrared Spectroscopy. *Biophys. J.* **1996**, *71* (4), 1796–1805.
- (54) Hansen, W. N. Electric Fields Produced by the Propagation of Plane Coherent Electromagnetic Radiation in a Stratified Medium. *J. Opt. Soc. Am.* **1968**, *58* (3), 380–388.
- (55) Iler, R. K. *The Chemistry of Silica: Solubility, Polymerization, Colloid and Surface Properties, and Biochemistry*; Wiley: New York, 1979.
- (56) Bucur, C. B.; Sui, Z.; Schlenoff, J. B. Ideal Mixing in Polyelectrolyte Complexes and Multilayers: Entropy Driven Assembly. *J. Am. Chem. Soc.* **2006**, *128* (42), 13690–13691.
- (57) Volodkin, D.; von Klitzing, R. Competing Mechanisms in Polyelectrolyte Multilayer Formation and Swelling: Polycation–Polyanion Pairing vs. Polyelectrolyte–Ion Pairing. *Curr. Opin. Colloid Interface Sci.* **2014**, *19* (1), 25–31.
- (58) Liu, C.; Thormann, E.; Claesson, P. M.; Tyrode, E. Surface Grafted Chitosan Gels. Part II: Gel Formation and Characterization. *Langmuir*. **2014**, DOI: 10.1021/la501319r.